crystals

MDPI

Article

Dual-Channel Underwater Acoustic Topological Rainbow Trapping Based on Synthetic Dimension

Jialin Zhong [1], Li Luo [1], Jiebin Peng [1], Yingyi Huang [1], Quanquan Shi [1], Jiajun Lu [1], Haobin Zhang [1], Feiwan Xie [2], Fugen Wu [3], Xin Zhang [1,*] and Degang Zhao [4,*]

[1] School of Physics and Optoelectronic Engineering, Guangdong University of Technology, Guangzhou 510006, China; 3217007281@mail2.gdut.edu.cn (J.Z.); luoliphys@gdut.edu.cn (L.L.); jiebin.peng@gdut.edu.cn (J.P.); yyhuang@gdut.edu.cn (Y.H.); 1112315001@mail2.gdut.edu.cn (Q.S.); 2112215097@mail2.gdut.edu.cn (J.L.); 2112215008@mail2.gdut.edu.cn (H.Z.)
[2] School of International Education, Guangdong University of Technology, Guangzhou 510006, China; 3221009857@mail2.gdut.edu.cn
[3] School of Materials and Energy, Guangdong University of Technology, Guangzhou 510006, China; wufg@gdut.edu.cn
[4] School of Physics, Huazhong University of Science and Technology, Wuhan 430074, China
* Correspondence: phxzhang@gdut.edu.cn (X.Z.); dgzhao@hust.edu.cn (D.Z.)

Abstract: The concept of "rainbow trapping" has generated considerable interest in wave propagation and energy harvesting, offering new possibilities for diverse and efficient acoustic wave operations. In this work, we investigate a dual-channel topological rainbow trapping device implemented within an underwater two-dimensional phononic crystal based on synthetic dimension. The topological edge states with different frequencies are separated and trapped at different spatial locations. Acoustic waves propagate simultaneously along two boundaries due to the degeneracy of the edge states. In particular, the propagation of a dual-channel topological rainbow is also realized by using a bend design. This work contributes to the advancement of multi-channel devices in synthetic space and provides a reference for the design of highly efficient underwater acoustic devices.

Keywords: phononic crystal; edge states; synthetic dimension; topological rainbow trapping

Citation: Zhong, J.; Luo, L.; Peng, J.; Huang, Y.; Shi, Q.; Lu, J.; Zhang, H.; Xie, F.; Wu, F.; Zhang, X.; et al. Dual-Channel Underwater Acoustic Topological Rainbow Trapping Based on Synthetic Dimension. *Crystals* **2024**, *14*, 311. https://doi.org/10.3390/cryst14040311

Academic Editor: Luis M. Garcia-Raffi

Received: 1 March 2024
Revised: 22 March 2024
Accepted: 25 March 2024
Published: 27 March 2024

1. Introduction

In recent years, the topological design of materials has provided a new paradigm for developing next-generation devices as well as a platform for the discovery of new physics [1,2]. Numerous implementations in mechanical [3], microwave [4], acoustic [5,6], and optical systems [7,8] have demonstrated the robustness of topological states against disorder, opening up new opportunities for developing devices with topologically protected functionality. Recently, topological properties in systems with additional degrees of freedom have also been explored, particularly within the setting of synthetic space, a higher-dimensional space constructed by the combination of physical and geometric dimensions [9,10]. The realization of synthetic dimensions broadly falls into two categories: one is to form an artificial lattice by designing couplings between various modes and the other is to introduce system-dependent parameters to explore higher-dimensional physical phenomena [11,12]. The synthetic dimension idea has expanded the realm of topological physics in various fields, such as photonics [13–15], acoustics [16], quantum systems [17,18], ultracold atoms [19], etc. This enables the observation of many novel high-dimensional phenomena and brings new opportunities to manipulate the internal degrees of freedom of a system.

Rainbow trapping, which separates and traps waves of different frequencies at different spatial positions, is advantageous for applications that require temporary energy storage [20,21], augmented energy–matter interaction [22,23], and efficient frequency

routing in classical systems [24–26]. Inspired by rainbow trapping, which originated from studies in electromagnetic waves [20,27–30], research has also been conducted on trapping acoustic waves. Zhu et al., achieved rainbow trapping of acoustic waves through spatial modulation of sound velocity in a new class of anisotropic metamaterials [31]. Guan et al., presented a method of controlling the propagation velocity of topological edge states through on-site potential and realized a prototype topological rainbow concentrator [32]. Wang et al., designed two different topological rainbow devices based on Valley Hall insulators exploiting rotation operation and boundary truncation [33]. Rainbow trapping along the boundary or interface of a single channel has been extensively studied and has achieved impressive results [34–37]. Water is another important sound medium in addition to solids and air, making it important to realize the acoustic topological insulators in a water background. Despite the advances in controlling acoustic waves in the air, multichannel rainbow trapping in aqueous environments remains largely unexplored to the best knowledge of the authors.

In this work, we establish a topological acoustic underwater dual-channel rainbow trapping device utilizing rotation deformation as the synthetic dimension. Rectangular scatterers are used to achieve a topological phononic crystal and a trivial phononic crystal in a honeycomb structure that can be converted to each other by rotating. Unlike the previous works of single-channel devices that relied on an isolated edge state, the rainbow trapping device in this study supports the topologically protected edge modes with twofold degeneracy. In a certain angular range, the frequencies of the nontrivial edge states decrease monotonically with the increase of the rotation angle. Therefore, an angular-gradient phononic crystal device can be constructed to realize topological rainbow trapping, enabling acoustic waves to propagate at different locations along the boundaries with changing frequencies. Moreover, the rainbow trapping device supports effective transmission at curved boundaries and is immune to scattering due to topological protection. This work provides some insights into the design of topological acoustic devices based on the synthetic dimension and has potential applications for underwater research on spatial wave filtering, energy harvesting, and acoustofluidics.

2. Structural Design and Band Inversion

In this paper, we begin by presenting a two-dimensional (2D) phononic crystal, composed of six rectangular pillars arranged in a honeycomb lattice. These pillars made of cork are immersed in water, as illustrated in Figure 1a, where the base vectors $\vec{a}_1 = (a, 0, 0)$ and $\vec{a}_2 = (\frac{1}{2}a, \frac{\sqrt{3}}{2}a, 0)$ are represented by red dashed lines in real space. In Figure 1b, $\vec{b}_1 = (0, \frac{4\pi}{\sqrt{3}a}, 0)$ and $\vec{b}_2 = (\frac{2\pi}{a}, -\frac{2\pi}{\sqrt{3}a}, 0)$ are base vectors in reciprocal space. The mass density and the wave velocity of the rectangular scatterers are 250 kg/m^3 and 489.9 m/s, respectively [38–40]. For water, the mass density is 1000 kg/m^3 and the sound velocity is 1490 m/s. Consider a rectangular pillar with a length and width of $0.25a \times 0.1a$, where the lattice constant is $a = 28\,\text{mm}$. The distance between the center of each rectangular pillar and the centroid of the unit cell is r, which satisfies $r = a/3$. Here, the counterclockwise (clockwise) rotation of the scatterer is defined as $\theta > 0$ ($\theta < 0$), which provides a degree of freedom for topological band manipulation. With an arbitrary rotation angle θ, the unit cell of the two-dimensional phononic crystal always maintains the C_6 symmetry.

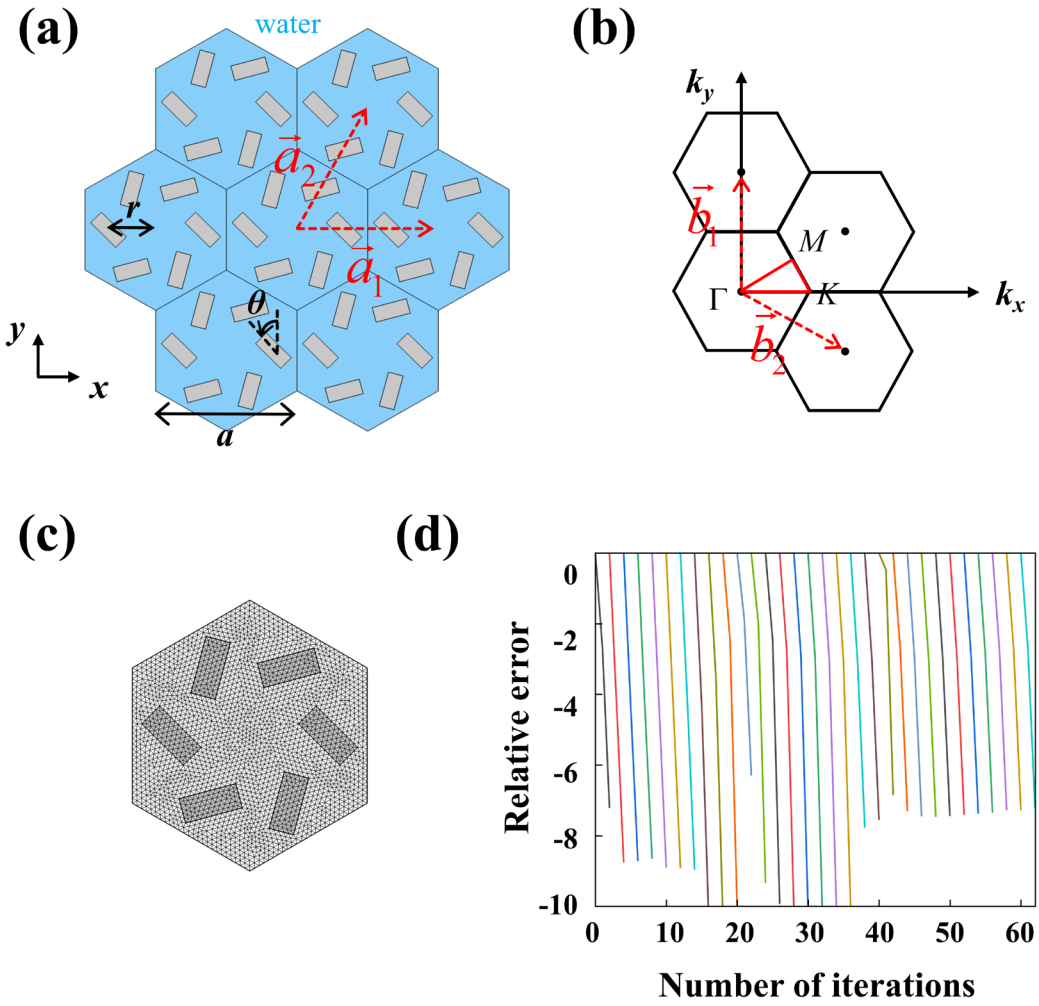

Figure 1. (**a**) Schematic diagram of unit cell composed of rectangular pillars with $\theta = 45°$, where blue areas indicate water. (**b**) Schematic diagram of reciprocal space and basis vector. (**c**) Finite element model of the two-dimensional phononic crystal. (**d**) Convergence graph during simulation (*y*-axis logarithmic scale).

Throughout this study, we employed the commercial finite-element software COMSOL Multiphysics to perform the calculations, including the band structures and field distributions. Using the pressure acoustic physics field, we selected the quadratic Lagrange element as the meshing element type in two-dimensional modeling. As shown in Figure 1c, the number of finite elements is 4608. The average cell mass is 0.9069 (the closer to 1, the better the mesh quality). A convergence graph during simulation is shown in Figure 1d. Each line segment in the convergence graph represents one iteration of the process. When all the computational errors are within the given range, the simulation proceeds to the next iteration. The relative tolerance we set for the system is 1.0×10^{-6} . It can be seen that each computational error shows a decreasing trend, and the minimum values of the line segments are smaller than the relative tolerance (−6), indicating that the mesh is converging.

According to the literature [41–43], there are two 2D irreducible representations at the Γ point of the Brillouin zone associated with the C_6 point group symmetry: E_1 and E_2, corresponding to the odd and even spatial parity, respectively. Figure 2a shows the band structures with $\theta = 0°$ (left), $\theta = 45°$ (middle), and $\theta = 90°$ (right), where the gray area marks the complete band gap. It is worth noting that we only consider the calculation of bands without fluid–solid interaction. There are two double-degeneracy points at the Γ point, one of which is the dipole mode and the other is the quadrupole mode,

referred to as the *p*-states and *d*-states, respectively. From the distributions of the eigenfields shown in Figure 2c, it is easy to recognize that the band inversion between the *p*-states and the *d*-states at the Γ point and the E_1 and E_2 representations have the same symmetry [41,44] as the (p_x, p_y) and $(d_{x^2-y^2}, d_{xy})$ orbitals of electrons in quantum systems, respectively. The two degenerate *p*-states have opposite parity with respect to the mirroring operations on the *x*-axis and *y*-axis, while the two degenerate *d*-states have the same parity with respect to the mirroring operations on the *x*-axis and *y*-axis. In Figure 2b, the distribution of the Dirac points indicated by red and green spheres in the synthetic space is depicted, with the *z*-axis representing the rotation angle ranging from 0 to 180 degrees. The pink and pale green horizontal planes represent the planes of $\theta = 45°$ and $\theta = 135°$, respectively. Thus, the coordinates of two Dirac points are $(0, 0, 45°)$ and $(0, 0, 135°)$. The angle for the topological transition occurs at $\theta = 45°$, where the intra- and intercluster couplings are equivalent and a double Dirac cone is formed [45,46]. Figure 2d illustrates the simulated eigenfrequencies of the *p*-states and *d*-states at the Γ point as a function of θ. More specifically, the relative eigenfrequencies corresponding to *d*-states are higher than those of *p*-states in the gray area, but are lower in the pink area, indicating that a band inversion process occurs as the θ of the rectangular pillars changes. For brevity, all frequencies have been normalized throughout this work.

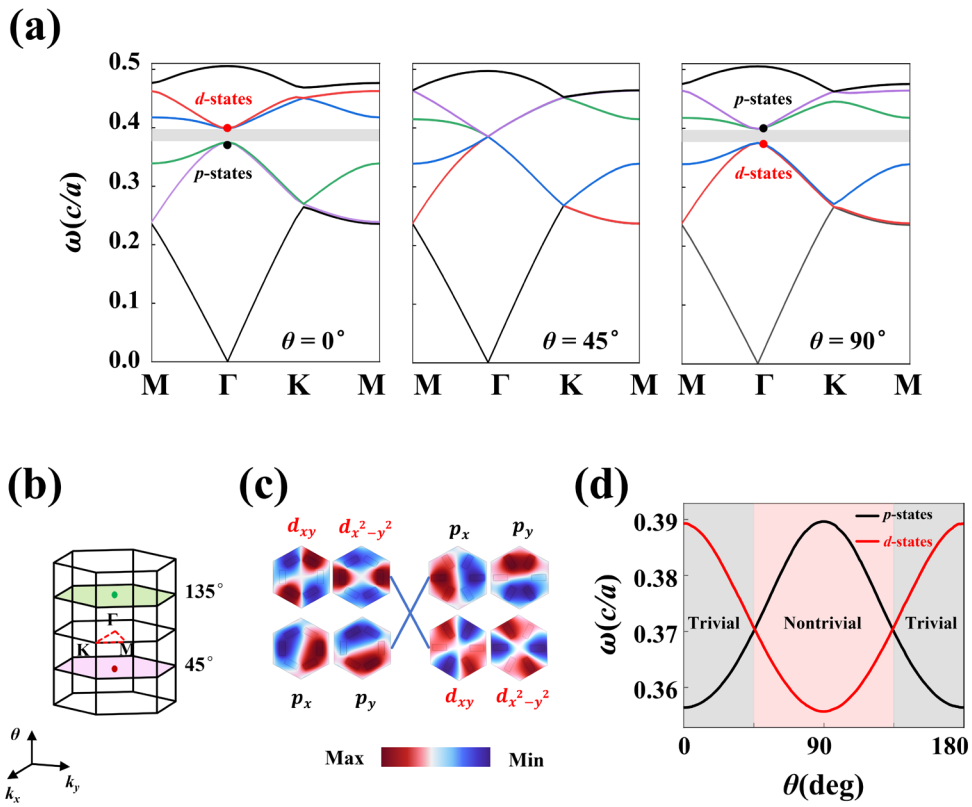

Figure 2. (**a**) Band structure diagrams with different parameters, and band gaps are marked in gray. (**b**) Distributions of Dirac points in synthetic space. (**c**) Pressure field distributions at the Γ point with $\theta = 0°$ and $\theta = 90°$, respectively. (**d**) Eigenfrequencies of *p*-states (black) and *d*-states (red) at Γ point.

3. Effective Hamiltonian and Chern Number

As mentioned before, the rotation angle has a period of π. The C_6 point symmetry group allows for the occurrence of a double degenerate Dirac cone at the Γ point, and a band inversion takes place upon rotating the rectangular pillars in the system [45,47]. The

band gap experiences processes of closing and reopening at the Dirac point. Through hybridizing *p*-states and *d*-states, the two pseudospin states are given by $p_{\pm} = (p_x \pm ip_y)/2$, $d_{\pm} = (d_{x^2-y^2} \pm id_{xy})/2$. To understand the topological property of the band gaps, a Hamiltonian near the Dirac point can be obtained using the $k-p$ perturbation method [48–50]:

$$H_{ij}^{eff} = H_{ij}' + \sum_n \frac{H_{in}' H_{nj}'}{\varepsilon_i - \varepsilon_n}, (i,j = 1,2,3,4) \tag{1}$$

where $H_{ij}' = \langle \Gamma_i | H' | \Gamma_j \rangle$ is the overlapping integral between different eigenstates Γ_i and Γ_j. We assume that $\Gamma_n (n = 1,2,3,4)$ are the four eigenstates at the Γ point: $\Gamma_1 = p_x$, $\Gamma_2 = p_y$, $\Gamma_3 = d_{x^2-y^2}$, $\Gamma_4 = d_{xy}$, and $\varepsilon_{1,2} = \varepsilon_p$, $\varepsilon_{3,4} = \varepsilon_d$ are the eigenfrequencies of the four pseudospin multipole modes at Γ. Rewriting the above Hamiltonian on the new base vector $[p_+, d_+, p_-, d_-]$, the effective Hamiltonian in the vicinity of the Γ point reduces to [51]:

$$H^{eff} = \begin{pmatrix} M - Bk^2 & Ak_+ & 0 & 0 \\ A^* k_- & -M + Bk^2 & 0 & 0 \\ 0 & 0 & M - Bk^2 & Ak_- \\ 0 & 0 & A^* k_+ & -M + Bk^2 \end{pmatrix} \tag{2}$$

where $k_{\pm} = k_x \pm ik_y$, $M = (\varepsilon_d - \varepsilon_p)/2$ is the frequency difference between *d*-states and *p*-states at Γ. The coefficients A are determined by the non-diagonal elements in the first-order perturbation term. The parameter B is obtained from the diagonal elements of the second-order perturbation term $H_{in}' H_{nj}'$, which is usually negative, i.e., $B < 0$. As a counterpart of the quantum spin Hall effect, the pseudospin Chen number of this acoustic system is denoted by C_s, which can be expressed as [52,53]:

$$C_s = \pm \frac{1}{2} \left[\mathrm{sgn}(M) + \mathrm{sgn}(B) \right] \tag{3}$$

when $BM < 0$, $C_s = 0$ corresponds to the trivial systems, while $BM > 0$, $C_s = \pm 1$ corresponds to the nontrivial state. In fact, as we can see in Figure 2, for the case ($\theta < 45°$ and $\theta > 135°$), the frequency of the dipole modes is lower than the frequency of the quadrupole modes. We obtain $C = 0$, which corresponds to a trivial phononic crystal. On the other hand, for the case $(45° < \theta < 135°)$, we obtain $C = \pm 1$, which corresponds to a topological nontrivial phononic crystal. It is further demonstrated that the system we designed undergoes a topological phase transition at different rotation angles.

4. Dispersion Analysis and Synthetic Virtual Space

Acoustic topological insulators exhibit unconventional edge states with topological protection [54], backward scattering suppression [55], and defect immunity [56]. As shown in Figure 3a, we designed a supercell composed of 12 nontrivial unit cells ($\theta = 80°$), circled by the red dashed line. Compared with the supercell of previous research, our proposed supercell is not formed by piecing trivial and nontrivial phononic crystals together. When $\theta = 80°$, the projected band diagram of lattices is given in Figure 3b. Two edge states appear in the band gap, which are represented by a solid blue line and a cyan dotted line corresponding to the upper and lower edge states, respectively. It is noteworthy that the edge states are always degenerate, which is related to the boundary truncation of the supercell. Due to the fact that the supercell is not spliced by trivial and topological regions, the dispersion curve lies close to the vicinity of one of the bulk bands instead of connecting the upper bulk band at one end and the lower bulk band at the other.

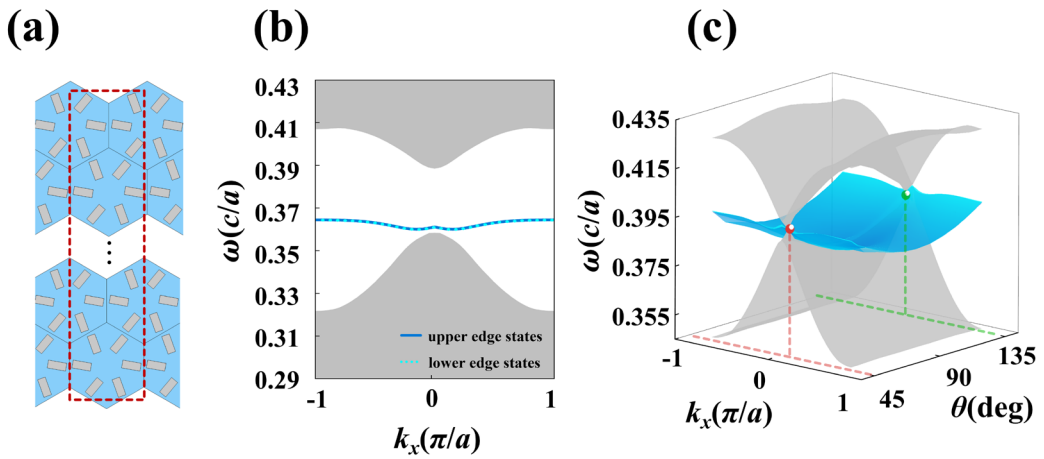

Figure 3. (**a**) Schematic of the supercell configuration $\theta = 80°$. (**b**) The edge states of the supercell are demonstrated by the red dashed frame in (**a**). (**c**) The projected surface dispersion of the synthetic space (k_x, θ). The surface mixed with blue and cyan represents the edge states, while the gray surfaces indicate the bulk states, in which the red and green spheres label the Dirac points.

The structure parameter θ is an important factor leading to different dispersion relations in two-dimensional phononic crystals. We investigate the dispersion of a series of supercells by changing the rotation angle. Figure 3c shows the projected band structure in synthetic space (k_x, θ), with the surfaces blended with blue and cyan denoting the degenerate edge states that connect two Dirac points. The edge states evolve with different parameters, and the rotation angle θ is able to change the dispersion relations of the honeycomb lattice phononic crystals, which can be regarded as an additional degree of freedom.

Most previous discussions on rainbow trapping have paid less attention to edge states with two-fold degeneracy [33,57–60]. In this work, the edge states are degenerate, which is determined by the boundary truncation of the supercell. As a general rule, the dispersion relations are symmetric with respect to the line $k_x = 0$. Hence, we only focus on one half of the dispersion relations, either the left or the right. An enlargement of the dispersion relation within $[0.2,1](\pi/a)$ is depicted in Figure 4a, where the rotation angles θ are selected as $50°$, $55°$, $60°$, $65°$, $70°$, and $80°$, respectively. At $k_x = 1(\pi/a)$, it can be observed that the frequencies of the degenerate edge states decrease monotonically as the rotation angles increase. The group velocities (near to zero) of the edge states are plotted as a function of frequency and rotation angle, as shown in Figure 4b. For each frequency, there are two extreme values of θ beyond which the system no longer supports any edge state. The unoccupied regions on the left and right correspond to frequencies where no edge states exist, while the edge states reside within the central colored region. Two blue dashed lines delineate the boundaries of these three regions, corresponding to the minima or maxima of the dispersion bands for a given rotation angle. Low group velocities allow the energy of the wave to converge, providing a stronger constraint on the propagation of sound waves [61]. The propagating sound can stop when the group velocity decreases to zero. This dispersion property enables separating topological edge states of different frequencies and trapping acoustic waves at a particular location along the direction of propagation to achieve a topological acoustic rainbow.

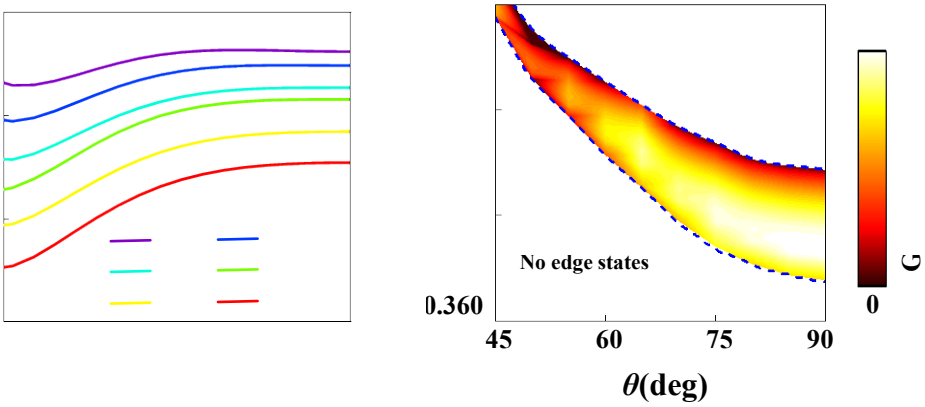

Figure 4. (**a**) The dispersion relations of the edge states at different rotation angles. (**b**) The group velocity distribution in synthetic space. The blue dashed lines denote the boundary between regions where the edge states exist and do not exist5. Topological Rainbow Device.

To investigate acoustic rainbow trapping, we designed a rainbow device composed of phononic crystals with different rotation angles. The rotation angle is spatially linearly modulated. Here, we define the parameter θ of the n-th column (in the x direction) as $\theta_{(n)}$:

$$\theta_{(n)} = \theta_1 + \frac{(\theta_N - \theta_1)(n-1)}{N-1}, 1 < n < N \tag{4}$$

where N is the total number of columns of the device, and θ_1 and θ_n are the rotation angles of the phononic crystals in the first and n-th columns, respectively. Spatial modulation leads to a specific angular arrangement of the phononic crystals within each column. The operating frequency range of a topological rainbow relies on the frequency range of edge states. As shown in Figure 5a, the gradient phononic crystal device we designed has $N = 19$ columns. The hard boundary conditions are imposed on the upper and lower boundaries. We set the parameters for the first and last columns to $\theta_1 = 45°$ and $\theta_N = 90°$, respectively. The rotation interval is $\Delta\theta = (\theta_N - \theta_1)/(N-1) = 2.5°$.

In practice, 3D printing technology facilitates precise control over sample accuracy and minimizes parametric errors [62,63]. Printed phononic crystal mounting plates allow for pre-tuning by designing the rotation angle of the phononic crystals before operation. Actually, there are some inevitable errors in the angular control, which could influence the integrity of the gradient phononic crystal configuration. We consider two scenarios involving such errors. In one scenario, the errors are substantial enough to disrupt the C_6 symmetry or the gradient arrangement of the phononic crystal. In such cases, the relationship between the rotational angle and dispersion of the edge states is not satisfied as discussed above, leading to the disruption of the rainbow effect. In the second scenario, the errors are within acceptable limits, $\Delta\theta < 2.5°$. Under this condition, the gradient phononic crystal structure still maintains a monotonic arrangement, meaning that the rainbow effect persists even if there is no significant change in the propagation distance. In addition, due to topological protection, the acoustic rainbow effect is immune to external perturbations, as will be discussed later.

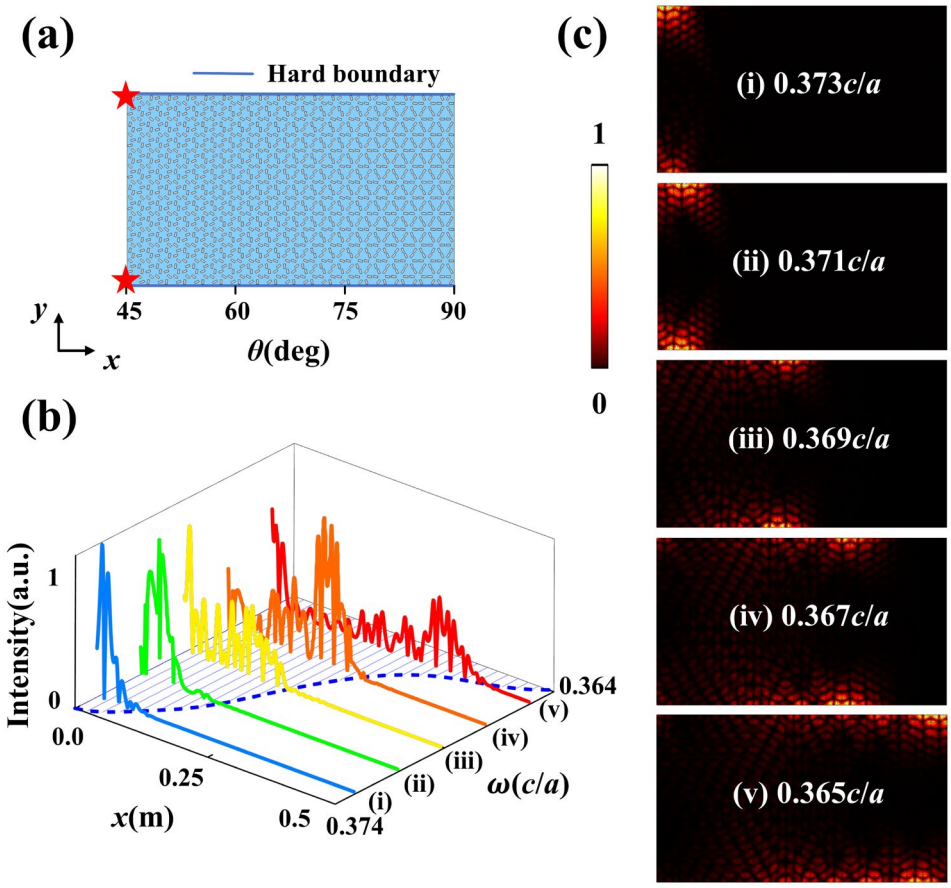

Figure 5. (**a**) Schematic of the dual-channel topological rainbow device. Solid blue lines indicate the imposition of hard boundary conditions and red pentagrams denote the positions of sound sources. (**b**) Normalized energy distributions along the boundaries. (**c**) Total pressure field distributions of edge states along x-axis that correlate with the frequencies labeled in Roman numerals in (**b**).

From Equation (4), the rotation angle of the acoustic dual-channel topological rainbow device monotonically increases from 45° to 90° along the θ-axis, as shown in Figure 5a. The normalized intensity distribution along the boundary is depicted in Figure 5b, where the x-axis denotes the propagation distances along the boundaries while the z-axis represents the normalized acoustic intensity. The total pressure field distributions for five frequencies are depicted in Figure 5c, with these frequencies labeled in Roman numerals in Figure 5b. The presence of the degenerate edge states results in equal excitation of both the upper and lower boundaries at the same frequency. We observe that the acoustic wave propagates along the upper and lower boundaries of the device and the propagation distances along the boundaries become longer and longer with the decrease in frequency. The property of edge states with a monotonic frequency shift within the bulk gap plays a key role in devising topological rainbow trapping. These results indicate that our acoustic gradient device achieves underwater topological rainbow trapping with dual boundary channels. For clarity, we varied the frequencies of the sound sources from higher to lower.

Energy losses play an important role in the wave propagation properties of phononic crystals. In a real three-dimensional space, due to the radiation losses, acoustic waves will be progressively dissipated in the direction perpendicular to a two-dimensional plane, that is, along the z-axis. The two-component phononic crystals are periodically arranged to form systems with spatially non-uniform material parameter distributions, where transverse and longitudinal modes and a mixture of these modes exist at the interfaces of

the fluid–solid interactions [64]. In addition, the interaction between water and cork pillars gives rise to more modes at the Γ point, which differ from those illustrated in Figure 2c. The thermal viscous losses of acoustic energy also contribute to the attenuation of the acoustic wave propagation as a result of interactions at the liquid–solid interfaces [65–67]. These effects can be conceptualized as energy loss within the two-dimensional plane. To identify this energy loss, we introduce the imaginary part of the sound velocity into water, and its impact on the rainbow effect in gradient phononic crystals is depicted in Figure 6a. Losses in rectangular pillars are neglected compared to those in water. There are complex coupling effects between liquid and solid systems, which reduce the eigenfrequency of solid–liquid structures to a certain extent. Further, as acoustic waves propagate farther and farther, radiation losses attenuate the transmission of acoustic waves in the process, which is clearly shown in Figure 6b.

The propagation length of acoustic energy within gradient phononic crystals fundamentally correlates with the operating frequency, a key aspect in the rainbow trapping phenomenon. The effectiveness of this phenomenon is critically constrained by inherent energy loss mechanisms, notably acoustic–thermal viscous damping and complex fluid–solid interactions [68–70]. As any material inherently exhibits energy loss properties,, it is worthwhile to consider the energy loss when analyzing the actual experimental results. These challenges impede the practical utilization of the rainbow effect within underwater acoustic contexts, prompting the need for comprehensive, detailed assessments in future research.

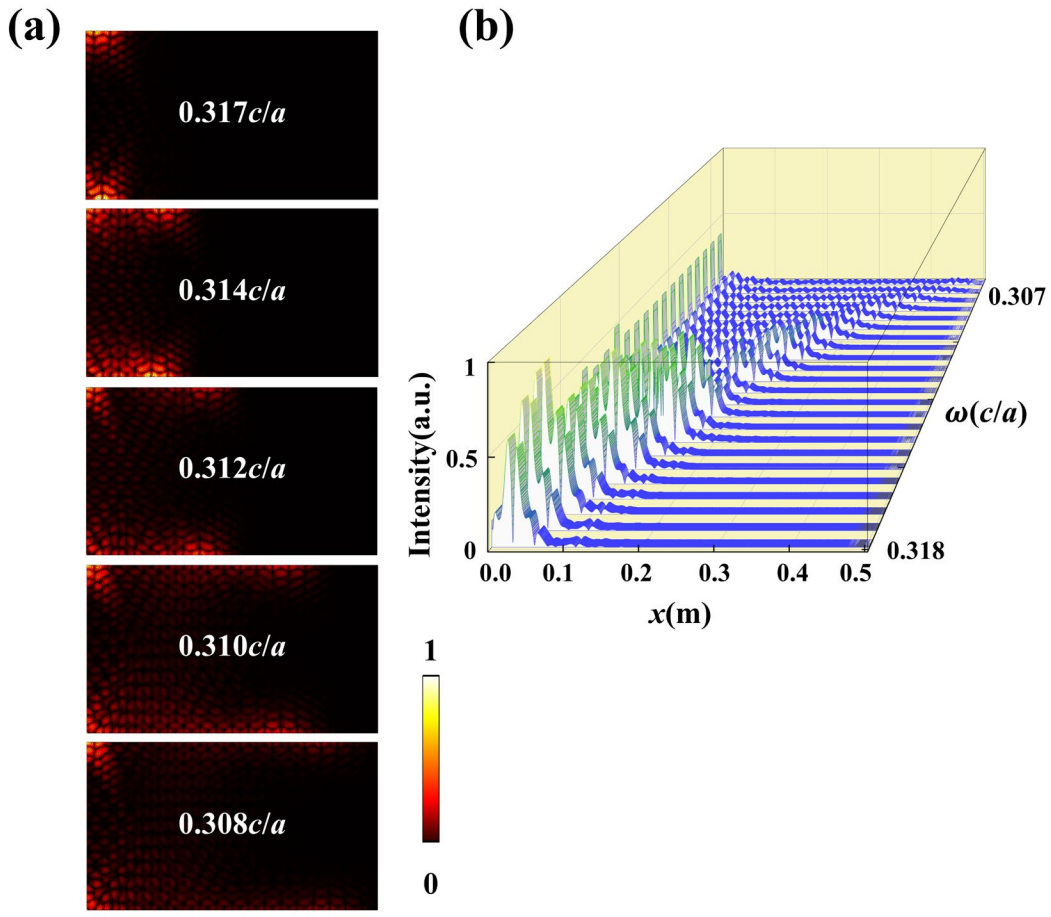

Figure 6. (**a**) Total pressure field distributions of edge states along *x*-axis with loss. (**b**) Normalized energy distributions along boundaries with energy loss.

Based on the above analysis, we demonstrate that the acoustic wave can be consistently transmitted on dual channels. It is important to note that the liquid and solid systems do not interact with each other in the ideal two-dimensional phononic crystal structure. In Figure 7a, we constructed a topological rainbow structure with a polygonal shape, where phononic crystals at the same θ were tilted in the direction indicated by the pink dashed line, forming two distinct curved channels and two corners A and B. As shown in Figure 7b, the sound waves propagate along two curved channels simultaneously. The incident acoustic wave at the frequency of 0.369*c*/*a* passes by corner A. Moreover, at a frequency of 0.367c/a, the acoustic wave passes by the corner B while the acoustic wave continues to propagate farther along another boundary. It can be noticed that the acoustic wave passes by the corners smoothly and the energy in the bulk is suppressed well. This finding enables us to design an expected curved boundary to realize flexible transportation of sound.

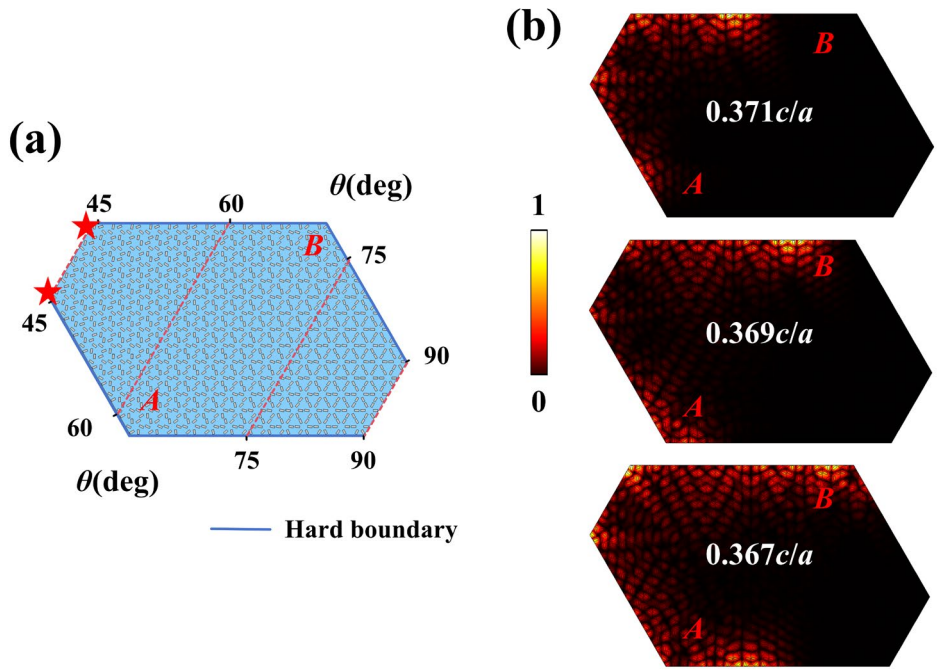

Figure 7. (**a**) Schematic diagram of a curved rainbow structure with the red pentagrams indicating the position of the acoustic sources. (**b**) The total pressure field distributions correspond to different frequencies.

5. The Robustness of the Topological Rainbow

In order to demonstrate the robustness of the topologically protected defect mode, some external perturbations are introduced in the proposed structure. As shown in Figure 8a, the rectangles near the boundaries were perturbed by rotational dislocation $\alpha = 45°$. Unlike the rotation angle θ for each column of the phononic crystal, α determines only the rotation angle of the perturbed rectangles here. Figure 8b shows that the incident wave at a frequency of 0.367*c*/*a* can pass through the defect position, which is circled by the yellowish dashed line. Clearly, the external rotation perturbations have little effect on the propagation of rainbow trapping.

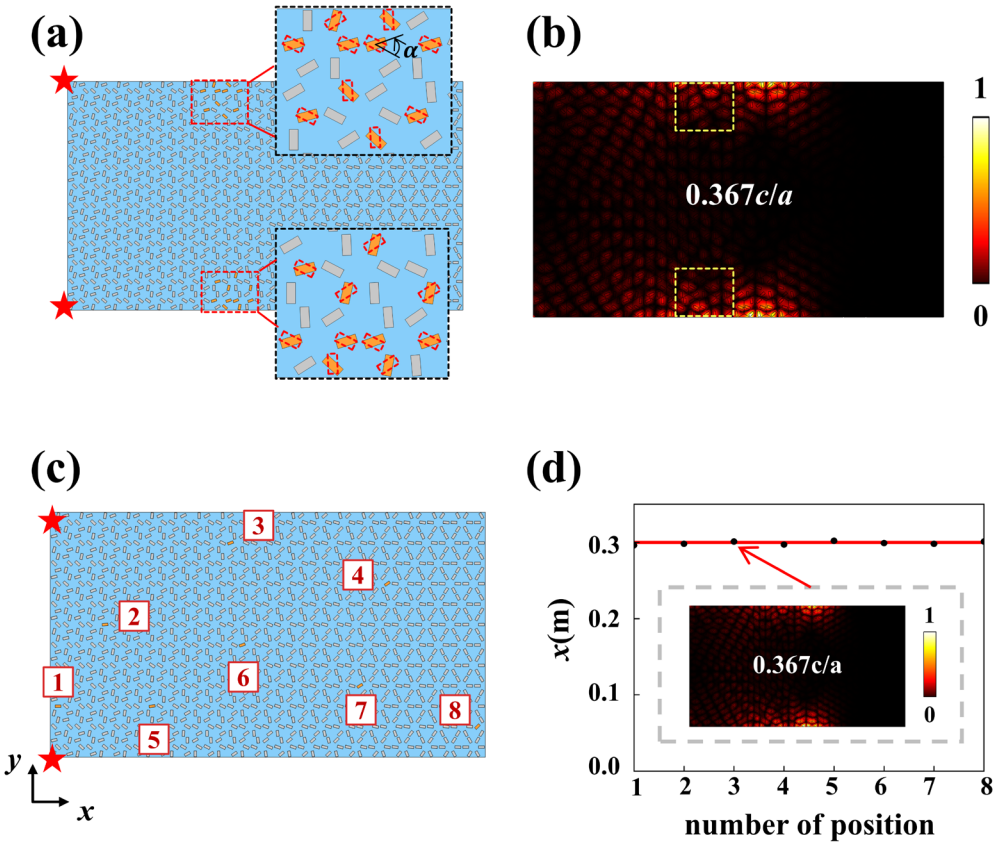

Figure 8. (**a**) Schematic of the topological structure with disorders in a close-up view. The red dashed lines represent the original locations of the rectangles, while the orange regions indicate their positions after perturbation. (**b**) Simulated acoustic pressure field with the disorders, which are encircled by the yellowish dashed line. (**c**) Schematic of a topological structure with randomly distributed disorders, labeled by numbers 1–8. (**d**) The evolution of propagation distances at a frequency of 0.367*c*/*a* with randomly located defects.

In addition to random rotational perturbations, the random locations of defects are introduced as well. Eight different defects are randomly introduced at positions marked by the labels in Figure 8c, each with a rotation perturbation of $\alpha = 45°$. Figure 8d illustrates the propagation distance of the topological rainbow appearing at a frequency of 0.367*c*/*a* with different locations of defects. The red line indicates that the acoustic wave propagates without any perturbation up to a distance of $x = 0.3\,\mathrm{m}$ at a frequency of 0.367*c*/*a*. We performed the simulation with the disorder at position 3 to obtain the acoustic pressure field distribution, as shown in the inset of Figure 8d. It is found that the propagation of the rainbow trapping is nearly unaffected by introducing a defect at any of these locations, and the propagation distances in the x direction are almost the same for all cases. Due to topological protection, the acoustic waves propagate along the boundaries even though the structure is destroyed by defects, demonstrating the robustness and advantage of our topological rainbow device for sound propagation.

6. Conclusions

In summary, we construct a phononic crystal device utilizing the rotation degree of freedom on the basis of rectangular pillars satisfying C_6 rotational symmetry. The synthesized Dirac points are realized in the synthesized space (k_x, k_y, θ), and a topological phase transition can be observed by using the band inversion mechanism. By modulating the rotation angle θ, the frequencies of the edge states can be shifted monotonically, and

we implement different propagation distances of acoustic waves for different frequencies in the gradient device. Simultaneous propagation of acoustic waves is observed along the upper and lower boundaries due to the degenerate dispersion curve of edge states. On the basis of our simulation test, we also verify the dual-channel propagation along the bending boundaries and the immunity to disorder. The topological rainbow trapping can be realized in a water background and provides a reference for further work on underwater acoustic devices in terms of safety and efficiency.

Author Contributions: Conceptualization, J.Z. and X.Z.; methodology, D.Z. and J.Z.; software, J.Z.; validation, J.Z., Q.S. and L.L.; formal analysis, Y.H. and H.Z.; investigation, J.P. and J.L.; resources, X.Z.; data curation, J.Z.; writing—original draft preparation, J.Z.; writing—review and editing, J.Z. and D.Z.; visualization, F.X. and J.L.; supervision, D.Z.; project administration, X.Z.; funding acquisition, F.W. and X.Z. All authors have read and agreed to the published version of the manuscript.

Funding: This work was supported by several research grants from the National Natural Science Foundation of China (grant no. 12274095; grant no. 12304057).

Data Availability Statement: Data available from the authors upon reasonable request.

Acknowledgments: We thank Xiying Fan (X.F.) for her help with simulations and Meng Xiao (M.X.) for helpful discussions.

Conflicts of Interest: The authors declare no conflict of interest.

References

1. Ma, G.; Xiao, M.; Chan, C.T. Topological phases in acoustic and mechanical systems. *Nat. Rev. Phys.* **2019**, *1*, 281–294. https://doi.org/10.1038/s42254-019-0030-x.
2. Zhang, X.; Zangeneh-Nejad, F.; Chen, Z.-G.; Lu, M.-H.; Christensen, J. A second wave of topological phenomena in photonics and acoustics. *Nature* **2023**, *618*, 687–697. https://doi.org/10.1038/s41586-023-06163-9.
3. Süsstrunk, R.; Huber, S.D. Classification of topological phonons in linear mechanical metamaterials. *Proc. Natl. Acad. Sci. USA* **2016**, *113*, E4767–E4775. https://doi.org/10.1073/pnas.1605462113.
4. Wang, Z.; Chong, Y.; Joannopoulos, J.D.; Soljačić, M. Observation of unidirectional backscattering-immune topological electromagnetic states. *Nature* **2009**, *461*, 772–775. https://doi.org/10.1038/nature08293.
5. Tian, Z.; Shen, C.; Li, J.; Reit, E.; Bachman, H.; Socolar, J.E.S.; Cummer, S.A.; Jun Huang, T. Dispersion tuning and route reconfiguration of acoustic waves in valley topological phononic crystals. *Nat. Commun.* **2020**, *11*, 762. https://doi.org/10.1038/s41467-020-14553-0.
6. Lu, J.; Qiu, C.; Ke, M.; Liu, Z. Valley Vortex States in Sonic Crystals. *Phys. Rev. Lett.* **2016**, *116*, 093901. https://doi.org/10.1103/PhysRevLett.116.093901.
7. Hafezi, M.; Mittal, S.; Fan, J.; Migdall, A.; Taylor, J.M. Imaging topological edge states in silicon photonics. *Nat. Photonics* **2013**, *7*, 1001–1005. https://doi.org/10.1038/nphoton.2013.274.
8. Wang, H.; Gupta, S.K.; Xie, B.; Lu, M. Topological photonic crystals: A review. *Front. Optoelectron.* **2020**, *13*, 50–72. https://doi.org/10.1007/s12200-019-0949-7.
9. Celi, A.; Massignan, P.; Ruseckas, J.; Goldman, N.; Spielman, I.B.; Juzeliūnas, G.; Lewenstein, M. Synthetic Gauge Fields in Synthetic Dimensions. *Phys. Rev. Lett.* **2014**, *112*, 043001. https://doi.org/10.1103/PhysRevLett.112.043001.
10. Yuan, L.; Lin, Q.; Xiao, M.; Fan, S. Synthetic dimension in photonics. *Optica* **2018**, *5*, 1396–1405. https://doi.org/10.1364/OPTICA.5.001396.
11. Lustig, E.; Weimann, S.; Plotnik, Y.; Lumer, Y.; Bandres, M.A.; Szameit, A.; Segev, M. Photonic topological insulator in synthetic dimensions. *Nature* **2019**, *567*, 356–360. https://doi.org/10.1038/s41586-019-0943-7.
12. Price, H.M.; Ozawa, T.; Goldman, N. Synthetic dimensions for cold atoms from shaking a harmonic trap. *Phys. Rev. A* **2017**, *95*, 023607. https://doi.org/10.1103/PhysRevA.95.023607.
13. Dutt, A.; Lin, Q.; Yuan, L.; Minkov, M.; Xiao, M.; Fan, S. A single photonic cavity with two independent physical synthetic dimensions. *Science* **2020**, *367*, 59–64. https://doi.org/10.1126/science.aaz3071.
14. Zhou, X.-F.; Luo, X.-W.; Wang, S.; Guo, G.-C.; Zhou, X.; Pu, H.; Zhou, Z.-W. Dynamically Manipulating Topological Physics and Edge Modes in a Single Degenerate Optical Cavity. *Phys. Rev. Lett.* **2017**, *118*, 083603. https://doi.org/10.1103/PhysRevLett.118.083603.
15. Luo, X.-W.; Zhou, X.; Xu, J.-S.; Li, C.-F.; Guo, G.-C.; Zhang, C.; Zhou, Z.-W. Synthetic-lattice enabled all-optical devices based on orbital angular momentum of light. *Nat. Commun.* **2017**, *8*, 16097. https://doi.org/10.1038/ncomms16097.
16. Chen, H.; Zhang, H.; Wu, Q.; Huang, Y.; Nguyen, H.; Prodan, E.; Zhou, X.; Huang, G. Creating synthetic spaces for higher-order topological sound transport. *Nat. Commun.* **2021**, *12*, 5028. https://doi.org/10.1038/s41467-021-25305-z.
17. Kraus, Y.E.; Ringel, Z.; Zilberberg, O. Four-Dimensional Quantum Hall Effect in a Two-Dimensional Quasicrystal. *Phys. Rev. Lett.* **2013**, *111*, 226401. https://doi.org/10.1103/PhysRevLett.111.226401.

18. Ozawa, T.; Price, H.M. Topological quantum matter in synthetic dimensions. *Nat. Rev. Phys.* **2019**, *1*, 349–357. https://doi.org/10.1038/s42254-019-0045-3.
19. Eckardt, A.; Hauke, P.; Soltan-Panahi, P.; Becker, C.; Sengstock, K.; Lewenstein, M. Frustrated quantum antiferromagnetism with ultracold bosons in a triangular lattice. *Europhys. Lett.* **2010**, *89*, 10010. https://doi.org/10.1209/0295-5075/89/10010.
20. Tsakmakidis, K.L.; Boardman, A.D.; Hess, O. 'Trapped rainbow' storage of light in metamaterials. *Nature* **2007**, *450*, 397–401. https://doi.org/10.1038/nature06285.
21. Kurt, H.; Yilmaz, D. Rainbow trapping using chirped all-dielectric periodic structures. *Appl. Phys. B* **2013**, *110*, 411–417. https://doi.org/10.1007/s00340-012-5270-8.
22. Xu, Y.; Fu, Y.; Chen, H. Planar gradient metamaterials. *Nat. Rev. Mater.* **2016**, *1*, 16067. https://doi.org/10.1038/natrevmats.2016.67.
23. Davies, B.; Chaplain, G.J.; Starkey, T.A.; Craster, R.V. Graded Quasiperiodic Metamaterials Perform Fractal Rainbow Trapping. *Phys. Rev. Lett.* **2023**, *131*, 177001. https://doi.org/10.1103/PhysRevLett.131.177001.
24. Chen, J.; Liang, W.; Li, Z.-Y. Switchable slow light rainbow trapping and releasing in strongly coupling topological photonic systems. *Photon. Res.* **2019**, *7*, 1075–1080. https://doi.org/10.1364/PRJ.7.001075.
25. Hussein, M.; Hameed, M.F.O.; Areed, N.F.F.; Yahia, A.; Obayya, S.S.A. Funnel-shaped silicon nanowire for highly efficient light trapping. *Opt. Lett.* **2016**, *41*, 1010–1013. https://doi.org/10.1364/OL.41.001010.
26. Yuan, H.; Zhang, N.; Zhang, H.; Lu, C. A Multi-Channel Frequency Router Based on an Optimization Algorithm and Dispersion Engineering. *Nanomaterials* **2023**, *13*, 2133. https://doi.org/10.3390/nano13142133.
27. Gan, Q.; Ding, Y.J.; Bartoli, F.J. "Rainbow" Trapping and Releasing at Telecommunication Wavelengths. *Phys. Rev. Lett.* **2009**, *102*, 056801. https://doi.org/10.1103/PhysRevLett.102.056801.
28. Gan, Q.; Fu, Z.; Ding, Y.J.; Bartoli, F.J. Ultrawide-Bandwidth Slow-Light System Based on THz Plasmonic Graded Metallic Grating Structures. *Phys. Rev. Lett.* **2008**, *100*, 256803. https://doi.org/10.1103/PhysRevLett.100.256803.
29. Sharma, S.; Mondal, A.; Das, R. Infrared rainbow trapping via optical Tamm modes in an one-dimensional dielectric chirped photonic crystals. *Opt. Lett.* **2021**, *46*, 4566–4569. https://doi.org/10.1364/OL.437958.
30. Lu, C.; Wang, C.; Xiao, M.; Zhang, Z.Q.; Chan, C.T. Topological Rainbow Concentrator Based on Synthetic Dimension. *Phys. Rev. Lett.* **2021**, *126*, 113902. https://doi.org/10.1103/PhysRevLett.126.113902.
31. Zhu, J.; Chen, Y.; Zhu, X.; Garcia-Vidal, F.J.; Yin, X.; Zhang, W.; Zhang, X. Acoustic rainbow trapping. *Sci. Rep.* **2013**, *3*, 1728. https://doi.org/10.1038/srep01728.
32. Guan, A.-Y.; Yang, Z.-Z.; Yang, W.-J.; Li, S.-F.; Zou, X.-Y.; Cheng, J.-C. Controlling Sound Wave Propagation in Topological Crystalline Insulators and Rainbow-Trapping. *Phys. Rev. Appl.* **2022**, *18*, 044054. https://doi.org/10.1103/PhysRevApplied.18.044054.
33. Wang, Z.; Wang, Z.; Li, H.; Liu, Z.; Luo, J.; Huang, F.; Huang, J.; Wang, X.; Li, H.; Yang, H. Probing Two Distinct Types of Topological Rainbow Concentrators Related to the Acoustic Valley Hall Insulator in Synthesized Three-Dimensional Space. *Phys. Rev. Appl.* **2022**, *17*, 064002. https://doi.org/10.1103/PhysRevApplied.17.064002.
34. Ni, X.; Wu, Y.; Chen, Z.-G.; Zheng, L.-Y.; Xu, Y.-L.; Nayar, P.; Liu, X.-P.; Lu, M.-H.; Chen, Y.-F. Acoustic rainbow trapping by coiling up space. *Sci. Rep.* **2014**, *4*, 7038. https://doi.org/10.1038/srep07038.
35. Ding, F.; Mao, Y.; Shen, J.; Dai, X.; Xiang, Y. Simultaneous slow light and sound rainbow trapping in phoxonic crystals. *Opt. Lett.* **2022**, *47*, 5650–5653. https://doi.org/10.1364/OL.475372.
36. Tang, X.-L.; Ma, T.-X.; Wang, Y.-S. Topological rainbow trapping and acoustic energy amplification in two-dimensional gradient phononic crystals. *Appl. Phys. Lett.* **2023**, *122*, 112201. https://doi.org/10.1063/5.0138982.
37. Tian, Z.; Yu, L. Rainbow trapping of ultrasonic guided waves in chirped phononic crystal plates. *Sci. Rep.* **2017**, *7*, 40004. https://doi.org/10.1038/srep40004.
38. Billard, A.; Bauer, R.; Mothe, F.; Colin, F.; Deleuze, C.; Longuetaud, F. Vertical variations in wood basic density for two softwood species. *Eur. J. For. Res.* **2021**, *140*, 1401–1416. https://doi.org/10.1007/s10342-021-01402-y.
39. Sergi, C.; Sarasini, F.; Tirillò, J. The Compressive Behavior and Crashworthiness of Cork: A Review. *Polymers* **2022**, *14*, 134. https://doi.org/10.3390/polym14010134.
40. Maderuelo-Sanz, R.; Barrigón Morillas, J.M.; Gómez Escobar, V. Acoustical performance of loose cork granulates. *Eur. J. Wood Wood Prod.* **2014**, *72*, 321–330. https://doi.org/10.1007/s00107-014-0784-x.
41. Wu, L.-H.; Hu, X. Scheme for Achieving a Topological Photonic Crystal by Using Dielectric Material. *Phys. Rev. Lett.* **2015**, *114*, 223901. https://doi.org/10.1103/PhysRevLett.114.223901.
42. Yang, Y.; Xu, Y.F.; Xu, T.; Wang, H.-X.; Jiang, J.-H.; Hu, X.; Hang, Z.H. Visualization of a Unidirectional Electromagnetic Waveguide Using Topological Photonic Crystals Made of Dielectric Materials. *Phys. Rev. Lett.* **2018**, *120*, 217401. https://doi.org/10.1103/PhysRevLett.120.217401.
43. Zhu, X.; Wang, H.-X.; Xu, C.; Lai, Y.; Jiang, J.-H.; John, S. Topological transitions in continuously deformed photonic crystals. *Phys. Rev. B* **2018**, *97*, 085148. https://doi.org/10.1103/PhysRevB.97.085148.
44. Mei, J.; Chen, Z.; Wu, Y. Pseudo-time-reversal symmetry and topological edge states in two-dimensional acoustic crystals. *Sci. Rep.* **2016**, *6*, 32752. https://doi.org/10.1038/srep32752.
45. Chen, C.; Song, W.; Lin, Z.; Wu, S.; Zhu, S.; Li, T. Rotation-configured topological phase transition in triangle photonic lattices. *Phys. Rev. B* **2023**, *108*, 134119. https://doi.org/10.1103/PhysRevB.108.134119.

46. Wang, X.-X.; Hu, X. Reconfigurable topological waveguide based on honeycomb lattice of dielectric cuboids. *Nanophotonics* **2020**, *9*, 3451–3458. https://doi.org/10.1515/nanoph-2020-0146.
47. Jin, M.-C.; Chen, Z.-G.; Lu, M.-H.; Zhan, P.; Chen, Y.-F. Flat Landau levels and interface states in two-dimensional photonic crystals with a nodal ring. *Phys. Rev. B* **2024**, *109*, 054108. https://doi.org/10.1103/PhysRevB.109.054108.
48. Zhang, Z.; Wei, Q.; Cheng, Y.; Zhang, T.; Wu, D.; Liu, X. Topological Creation of Acoustic Pseudospin Multipoles in a Flow-Free Symmetry-Broken Metamaterial Lattice. *Phys. Rev. Lett.* **2017**, *118*, 084303. https://doi.org/10.1103/PhysRevLett.118.084303.
49. Li, Y.; Wu, Y.; Mei, J. Double Dirac cones in phononic crystals. *Appl. Phys. Lett.* **2014**, *105*, 014107. https://doi.org/10.1063/1.4890304.
50. Mei, J.; Wu, Y.; Chan, C.T.; Zhang, Z.-Q. First-principles study of Dirac and Dirac-like cones in phononic and photonic crystals. *Phys. Rev. B* **2012**, *86*, 035141. https://doi.org/10.1103/PhysRevB.86.035141.
51. Wu, S.; Wu, Y.; Mei, J. Topological helical edge states in water waves over a topographical bottom. *New J. Phys.* **2018**, *20*, 023051. https://doi.org/10.1088/1367-2630/aa9cdb.
52. Smirnova, D.; Leykam, D.; Chong, Y.; Kivshar, Y. Nonlinear topological photonics. *Appl. Phys. Rev.* **2020**, *7*, 021306. https://doi.org/10.1063/1.5142397.
53. Shen, S.-Q.; Shan, W.-Y.; Lu, H.-Z. Topological Insulator and the Dirac Equation. *SPIN* **2011**, *1*, 33–44. https://doi.org/10.1142/S2010324711000057.
54. Fan, X.; Xia, T.; Qiu, H.; Zhang, Q.; Qiu, C. Tracking Valley Topology with Synthetic Weyl Paths. *Phys. Rev. Lett.* **2022**, *128*, 216403. https://doi.org/10.1103/PhysRevLett.128.216403.
55. Xie, B.; Su, G.; Wang, H.-F.; Liu, F.; Hu, L.; Yu, S.-Y.; Zhan, P.; Lu, M.-H.; Wang, Z.; Chen, Y.-F. Higher-order quantum spin Hall effect in a photonic crystal. *Nat. Commun.* **2020**, *11*, 3768. https://doi.org/10.1038/s41467-020-17593-8.
56. He, C.; Ni, X.; Ge, H.; Sun, X.-C.; Chen, Y.-B.; Lu, M.-H.; Liu, X.-P.; Chen, Y.-F. Acoustic topological insulator and robust one-way sound transport. *Nat. Phys.* **2016**, *12*, 1124–1129. https://doi.org/10.1038/nphys3867.
57. Li, M.X.; Wang, Y.K.; Lu, M.J.; Sang, T. Dual-mode of topological rainbow in gradual photonic heterostructures. *J. Phys. D Appl. Phys.* **2022**, *55*, 095103. https://doi.org/10.1088/1361-6463/ac37df.
58. Lu, C.; Sun, Y.-Z.; Wang, C.; Zhang, H.; Zhao, W.; Hu, X.; Xiao, M.; Ding, W.; Liu, Y.-C.; Chan, C.T. On-chip nanophotonic topological rainbow. *Nat. Commun.* **2022**, *13*, 2586. https://doi.org/10.1038/s41467-022-30276-w.
59. Liu, J.; Lu, X.; Dai, X.; Xiang, Y. Rainbow trapping and releasing based on the topological photonic crystals and a gradient 1D array. *J. Appl. Phys.* **2022**, *132*, 173105. https://doi.org/10.1063/5.0118957.
60. Hayran, Z.; Kurt, H.; Staliunas, K. Rainbow trapping in a chirped three-dimensional photonic crystal. *Sci. Rep.* **2017**, *7*, 3046. https://doi.org/10.1038/s41598-017-03454-w.
61. Zhang, H.; Qian, L.; Wang, C.; Ji, C.-Y.; Liu, Y.; Chen, J.; Lu, C. Topological rainbow based on graded topological photonic crystals. *Opt. Lett.* **2021**, *46*, 1237–1240. https://doi.org/10.1364/OL.419271.
62. Zhang, X.; Liu, L.; Lu, M.-H.; Chen, Y.-F. Valley-Selective Topological Corner States in Sonic Crystals. *Phys. Rev. Lett.* **2021**, *126*, 156401. https://doi.org/10.1103/PhysRevLett.126.156401.
63. Li, J.; Deng, C.; Zhang, K.; Lu, Q.; Yang, H. Higher-order topological states in dual-band valley sonic crystals. *Appl. Phys. Lett.* **2023**, *123*, 253101. https://doi.org/10.1063/5.0180878.
64. Wu, X.; Fan, H.; Liu, T.; Gu, Z.; Zhang, R.-Y.; Zhu, J.; Zhang, X. Topological phononics arising from fluid-solid interactions. *Nat. Commun.* **2022**, *13*, 6120. https://doi.org/10.1038/s41467-022-33896-4.
65. Moiseyenko, R.P.; Laude, V. Material loss influence on the complex band structure and group velocity in phononic crystals. *Phys. Rev. B* **2011**, *83*, 064301. https://doi.org/10.1103/PhysRevB.83.064301.
66. Sprik, R.; Wegdam, G.H. Acoustic band gaps in composites of solids and viscous liquids. *Solid State Commun.* **1998**, *106*, 77–81. https://doi.org/10.1016/S0038-1098(98)00029-5.
67. Mukhin, N.; Kutia, M.; Aman, A.; Steinmann, U.; Lucklum, R. Two-Dimensional Phononic Crystal Based Sensor for Characterization of Mixtures and Heterogeneous Liquids. *Sensors* **2022**, *22*, 2816. https://doi.org/10.3390/s22072816.
68. Lou, J.; He, L.; Yang, J.; Kitipornchai, S.; Wu, H. Wave propagation in viscoelastic phononic crystal rods with internal resonators. *Appl. Acoust.* **2018**, *141*, 382–392. https://doi.org/10.1016/j.apacoust.2018.07.029.
69. Guo, W.; Zhang, S.-Y.; Wang, Y.-F.; Laude, V.; Wang, Y.-S. Evanescent Lamb waves in viscoelastic phononic metastrip. *Int. J. Mech. Sci.* **2022**, *236*, 107748. https://doi.org/10.1016/j.ijmecsci.2022.107748.
70. Pedersen, J.G.; Xiao, S.; Mortensen, N.A. Limits of slow light in photonic crystals. *Phys. Rev. B* **2008**, *78*, 153101. https://doi.org/10.1103/PhysRevB.78.153101.